

Quantum Optical Arbitrary Waveform Manipulation and Measurement in Real Time

Abijith S. Kowligy^{1,†}, Paritosh Manurkar^{1,†}, Neil V. Corzo¹, Vesselin G. Velev², Michael Silver¹, Ryan P. Scott³, S. J. B. Yoo³, Prem Kumar^{1,2}, Gregory S. Kanter¹, and Yu-Ping Huang^{1,2}

¹ *Department of Electrical Engineering and Computer Science, Northwestern University, Evanston, IL USA 60208-3118*

² *Department of Physics and Astronomy, Northwestern University, Evanston, IL USA 60208-3112*

³ *Department of Electrical and Computer Engineering, University of California, Davis, CA USA 95616*

Abstract: We describe a technique for dynamic quantum optical arbitrary-waveform generation and manipulation, which is capable of mode selectively operating on quantum signals without inducing significant loss or decoherence. It is built upon combining the developed tools of quantum frequency conversion and optical arbitrary waveform generation. Considering realistic parameters, we propose and analyze applications such as programmable reshaping of picosecond-scale temporal modes, selective frequency conversion of any one or superposition of those modes, and mode-resolved photon counting. We also report on experimental progress to distinguish two overlapping, orthogonal temporal modes, demonstrating over 8 dB extinction between picosecond-scale time-frequency modes, which agrees well with our theory. Our theoretical and experimental progress, as a whole, points to an enabling optical technique for various applications such as ultradense quantum coding, unity-efficiency cavity-atom quantum memories, and high-speed quantum computing.

© 2014 Optical Society of America

OCIS codes: 270.0720,270.5585,190.4410

References and links

1. M. B. Nasr, D. P. Goode, N. Nguyen, G. Rong, L. Yang, B. M. Reinhard, B. E. Saleh, and M. C. Teich, "Quantum optical coherence tomography of a biological sample," *Optics Communications* **282**, 1154–1159 (2009).
2. J. I. Cirac, P. Zoller, H. J. Kimble, and H. Mabuchi, "Quantum state transfer and entanglement distribution among distant nodes in a quantum network," *Phys. Rev. Lett.* **78**, 3221 (1997).
3. J.-W. Pan, Z.-B. Chen, C.-Y. Lu, H. Weinfurter, A. Zeilinger, and M. Żukowski, "Multiphoton entanglement and interferometry," *Rev. Mod. Phys.* **84**, 777–838 (2012).
4. A. V. Gorshkov, A. André, M. Fleischhauer, A. S. Sørensen, and M. D. Lukin, "Universal approach to optimal photon storage in atomic media," *Phys. Rev. Lett.* **98**, 123601 (2007).
5. Y.-Z. Sun, Y.-P. Huang, and P. Kumar, "Photonic nonlinearities via quantum zeno blockade," *Phys. Rev. Lett.* **110**, 223901 (2013).
6. S. T. Cundiff and A. M. Weiner, "Optical arbitrary waveform generation," *Nat Photon* **4**, 760–766 (2010).
7. Z. Jiang, C.-B. Huang, D. E. Leaird, and A. M. Weiner, "Optical arbitrary waveform processing of more than 100 spectral comb lines," *Nature Photonics* **1**, 463 (2007).
8. R. P. Scott, N. K. Fontaine, J. P. Heritage, and S. J. B. Yoo, "Dynamic optical arbitrary waveform generation and measurement," *Opt. Express* **18**, 18655–18670 (2010).

9. D. Geisler, N. Fontaine, R. Scott, J. Heritage, K. Okamoto, and S. J. B. Yoo, "360-gb/s optical transmitter with arbitrary modulation format and dispersion precompensation," *Photonics Technology Letters, IEEE* **21**, 489–491 (2009).
10. D. Goswami, "Optical pulse shaping approaches to coherent control," *Phys. Reports* **374**, 385 (2003).
11. J. M. Lukens, A. Dezfolyian, C. Langrock, M. M. Fejer, D. E. Leaird, and A. M. Weiner, "Orthogonal spectral coding of entangled photons," *Phys. Rev. Lett.* **112**, 133602 (2014).
12. J. Palací, A. Bockelt, and B. Vidal, "Terahertz radiation shaping based on optical spectrum modulation in the time domain," *Opt. Express* **20**, 23117–23125 (2012).
13. P. Kolchin, C. Belthangady, S. Du, G. Y. Yin, and S. E. Harris, "Electro-optic modulation of single photons," *Phys. Rev. Lett.* **101**, 103601 (2008).
14. R. W. Boyd, *Nonlinear Optics* (Academic Press, 2008).
15. G. P. Agrawal, *Nonlinear Fiber Optics* (Academic Press, Boston, 2007), 4th ed.
16. P. Kumar, "Quantum frequency conversion," *Opt. Lett.* **15**, 1476–1478 (1990).
17. B. Brecht, A. Eckstein, R. Ricken, V. Quiring, H. Suche, L. Sansoni, and C. Silberhorn, "The quantum pulse gate - enabling high-dimensional time-frequency quantum information," arXiv:1403.4397 [quant-ph] (2014).
18. D. V. Reddy, M. G. Raymer, C. J. McKinstrie, L. Mejling, and K. Rottwitt, "Temporal mode selectivity by frequency conversion in second-order nonlinear optical waveguides," *Opt. Express* **21**, 13840–13863 (2013).
19. Y.-P. Huang and P. Kumar, "Mode-resolved photon counting via cascaded quantum frequency conversion," *Opt. Lett.* **38**, 468–470 (2013).
20. D. Kielpinski, J. F. Corney, and H. M. Wiseman, "Quantum Optical Waveform Conversion," *Phys. Rev. Lett.* **106**, 130501 (2011).
21. J. Lavoie, J. Donohue, L. Wright, A. Fedrizzi, and K. J. Resch, "Spectral compression of single photons," *Nat Photon* **7**, 363–366 (2013).
22. M. Vasilyev and P. Kumar, "Frequency up-conversion of quantum images," *Opt. Express* **20**, 6644–6656 (2012).
23. J. Shapiro, "The quantum theory of optical communications," *Selected Topics in Quantum Electronics, IEEE Journal of* **15**, 1547–1569 (2009).
24. C. J. McKinstrie, L. Mejling, M. G. Raymer, and K. Rottwitt, "Quantum-state-preserving optical frequency conversion and pulse reshaping by four-wave mixing," *Phys. Rev. A* **85**, 053829 (2012).
25. C. Söller, B. Brecht, P. J. Mosley, L. Y. Zang, A. Podlipensky, N. Y. Joly, P. S. J. Russell, and C. Silberhorn, "Bridging visible and telecom wavelengths with a single-mode broadband photon pair source," *Phys. Rev. A* **81**, 031801 (2010).
26. A. Eckstein, B. Brecht, and C. Silberhorn, "A quantum pulse gate based on spectrally engineered sum frequency generation," *Opt. Express* **19**, 13770–13778 (2011).
27. F. M. Soares, N. K. Fontaine, R. P. Scott, J. Baek, X. Zhou, T. Su, S. Cheung, Y. Wang, C. Junesand, S. Lourduoss, K. Y. Liou, R. A. Hamm, W. Wang, B. Patel, L. A. Gruezeke, W. T. Tsang, J. P. Heritage, and S. J. B. Yoo, "Monolithic InP 100-channel x 10-ghz device for optical arbitrary waveform generation," *Photonics Journal, IEEE* **3**, 975–985 (2011).
28. N. K. Fontaine, R. P. Scott, and S. J. B. Yoo, "Dynamic optical arbitrary waveform generation and detection in InP photonic integrated circuits for Tb/s optical communications," *Optics Communications* **284**, 3693–3705 (2011).
29. C. E. Vollmer, C. Baune, A. Sambrowski, T. Eberle, V. Händchen, J. Fiurášek, and R. Schnabel, "Quantum up-conversion of squeezed vacuum states from 1550 to 532nm," *Phys. Rev. Lett.* **112**, 073602 (2014).
30. G. C. Valley, "Photonic analog-to-digital converters," *Optics Express* **15**, 1955–1982 (2007).
31. H. J. Kimble, "The quantum internet," *Nature* **453**, 1023–1030 (2008).
32. S. S. Rao, *Engineering Optimization: Theory and Practice* (Wiley Publishing, 2009).
33. Y.-P. Huang, J. B. Altepeter, and P. Kumar, "Optimized heralding schemes for single photons," *Phys. Rev. A* **84**, 033844 (2011).
34. V. Balić, D. A. Braje, P. Kolchin, G. Y. Yin, and S. E. Harris, "Generation of paired photons with controllable waveforms," *Phys. Rev. Lett.* **94**, 183601 (2005).
35. P. P. Rohde, T. C. Ralph, and M. A. Nielsen, "Optimal photons for quantum-information processing," *Phys. Rev. A* **72**, 052332 (2005).
36. R. Wu, V. R. Supradeepa, C. M. Long, D. E. Leaird, and A. M. Weiner, "Generation of very flat optical frequency combs from continuous-wave lasers using cascaded intensity and phase modulators driven by tailored radio frequency waveforms," *Opt. Lett.* **35**, 3234–3236 (2010).
37. P. S. Kuo, J. S. Pelc, O. Slattery, Y.-S. Kim, M. M. Fejer, and X. Tang, "Reducing noise in single-photon-level frequency conversion," *Opt. Lett.* **38**, 1310–1312 (2013).
38. Y.-P. Huang and P. Kumar, "Distilling quantum entanglement via mode-matched filtering," *Phys. Rev. A* **84**, 032315 (2011).
39. J. B. Altepeter, N. N. Oza, M. Medić, E. R. Jeffrey, and P. Kumar, "Entangled photon polarimetry," *Opt. Express* **19**, 26011–26016 (2011).
40. C. Polycarpou, K. N. Cassemiro, G. Venturi, A. Zavatta, and M. Bellini, "Adaptive detection of arbitrarily shaped ultrashort quantum light states," *Phys. Rev. Lett.* **109**, 053602 (2012).

1. Introduction

The past decades have witnessed tremendous advances of interdisciplinary fields via the use of exotic optical technology exploiting the nonclassical features of light waves to achieve performance elusive to their classical counterparts [1]. Practically, such technology needs to be accompanied by tools capable of manipulating and measuring the spatiotemporal modes of the quantum optical signals without introducing significant loss or background noise. This is particularly important for loss-sensitive quantum applications critically relying on the use of optical signals in custom-tailored modes [2, 3]. For example, photons in rising exponential pulses [4] are desired for efficient quantum-state transfer between light and matter waves. Also, optical pulses conjugate to the cavity leakage modes are required for strong interaction in $\chi^{(2)}$ -microresonator based quantum logic gates [5]. In this work, we present an all-optical realization of such tools.

Emergent technologies such as optical arbitrary waveform generation (OAWG) serve as an important tool for synthesis of user-specified optical waveforms with modulation bandwidths that can exceed the terahertz scale, eclipsing the ~ 20 GHz bandwidths of high performance electronic arbitrary waveform generators [6]. By providing the OAWG device with an optical frequency comb (OFC) with comb-spacing equal to or greater than the OAWG resolution, it is possible to control the amplitude and phase of each comb-line independently and dynamically, generating a waveform that is user-controlled over 100% of the comb period [7, 8]. Since its arrival, OAWG has profoundly impacted many subject areas of classical optics, including ultrahigh capacity optical communications [9] and broadband spectroscopy [10]. It is, however, challenging to transition this technology in its present form to the quantum domain because of the large insertion loss typically incurred, in addition to the inevitable modulation loss [11]. We note that OAWG devices using active gain are not applicable to quantum signals [12]. Such high losses or background noise levels can devastate quantum signals through decoherence and render single-photon states highly probabilistic and/or impure, making them unsuitable for quantum-optical applications particularly when on-demand quantum signals are desired.

Here, we present numerical and experimental evidence of a quantum optical technique capable of manipulating and measuring arbitrary optical waveforms in real time while, in principle, being lossless and free of background noise. Instead of direct modulation, where significant modulation loss would occur in addition to insertion loss [13], in our design the signals are manipulated through nonlinear optical frequency conversion processes tailored by shaped classical pump pulses. This eliminates otherwise inevitable high modulation/insertion loss for the quantum signals. The nonlinear processes can be sum-frequency generation (SFG) or difference-frequency generation (DFG) in $\chi^{(2)}$ media [14], or Bragg-scattering four-wave mixing in $\chi^{(3)}$ media [15]. These processes preserve the full quantum statistics of the input signal, allowing for applications such as quantum frequency conversion (QFC) where the carrier frequencies of photonic signals are translated without disturbing their quantum states, including any correlation or entanglement with other quantum objects [16]. By using appropriately shaped pump pulses via OAWG, it is possible to tailor the QFC process for realizing coherent operations on individual or on superpositions of quantum modes in arbitrary waveforms. Recently, dispersion-engineered waveguides have been used to discriminate Hermite-Gaussian time-frequency modes [17]. Also, using Gaussian pump-pulses of appropriate temporal widths, selective frequency conversion of certain temporal modes has been proposed [18]. In contrast, we utilize the OAWG device to generate custom-tailored pump pulses for selectively upconverting optical quantum states in arbitrary temporal profiles, without requiring any custom-engineered waveguide [19].

We analyze an example case where any of 10 modes or their superpositions can be selected by appropriately shaping the pump pulse. By passing a quantum signal sequentially through multiple QFC stages each driven by pump pulses generated via OAWG, we numerically demonstrate mode-resolved photon counting of the signal. Moreover, we show that high-efficiency, essentially lossless reshaping of quantum optical waveforms is also possible, which represents an essential resource for interfacing disparate architectures in networked quantum applications. While quantum optical waveform conversion using sum-frequency generation has been investigated theoretically [20] and experimentally [21], we show that finer, more general control of the pump shape via OAWG allows for substantially higher conversion efficiency ($> 90\%$) and high fidelity ($> 90\%$) waveform conversion, simultaneously. Moreover, these numerical studies have been performed by considering realistic parameters available in existing commercial devices. We emphasize that owing to the development of dynamic OAWG devices, those operations can be implemented in “real time,” i.e., the converted modes can be updated at a GHz rate or higher. This unique capability may lead to exciting applications in efficient secure information processing, particularly quantum key distribution using high-dimensional temporal modes.

The rest of the paper is organized as follows: in Section 2, we present the basic idea and propose an experimental setup for our approach. In Section 3 we review the dynamic OAWG technique and present some of our recent progress in this area. In Section 4, we outline three example applications of our proposal for high-fidelity measurement and manipulation of picosecond-scale temporal modes. In Section 5, we report on experimental progress towards developing such devices in a periodically-poled potassium titanyl phosphate (PPKTP) waveguide.

2. Theoretical Background

A basic implementation of our proposed technique is sketched in Fig. 1, where a $\chi^{(2)}$ nonlinear waveguide is employed. Similar implementations could be realized in other systems, such as silicon-family chip devices and optical fibers, the latter being drop-in compatible with the existing fiber-based telecommunication infrastructure. Our analysis below could be extended to those systems in a straightforward manner.

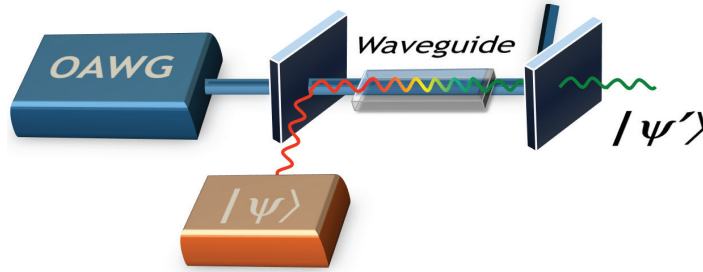


Fig. 1. QFC with tailored pump pulses.

In this paper, we focus on operations in the time domain while assuming the waveguide supports only a single spatial mode for each lightwave. Extending the present analysis to include spatial degrees of freedom is feasible [22] and will be presented elsewhere. Considering SFG, the nonlinear dynamics can be described by the coupled Heisenberg equations of motion

(assuming lossless propagation for all waves and in the undepleted pump regime),

$$(\partial_z + \sum_n \mu_n \partial_t^n) \hat{a}(z, t) = i\eta \Psi(t) \hat{b}(z, t), \quad (1a)$$

$$(\partial_z + \sum_n \nu_n \partial_t^n) \hat{b}(z, t) = i\eta^* \Psi^*(t) \hat{a}(z, t), \quad (1b)$$

which are derived in a moving frame traveling with the pump wave. Here, \hat{a} and \hat{b} are the annihilation operators for the sum-frequency (SF) and the signal waves, respectively, satisfying the standard commutation relations, viz., $[\hat{a}(z, t), \hat{a}^\dagger(z', t')] = \delta(z - z')\delta(t - t')$; η is a coefficient measuring the SFG strength; $\Psi(t)$ gives the temporal profile of the classical pump pulse; and μ_1 and ν_1 are the inverse group velocities of the signal and sum-frequency (SF) waves, respectively, in the pump moving frame, while μ_n and ν_n ($n \geq 2$) are their n -th order dispersions.

Equations (1) can be solved using the standard Green's function approach. When there is no input SF wave, the waveguide output at the SF wavelength can be obtained through the transformation relation, $\hat{a}(L, t) = \int dt' G_1(t, t') \hat{b}(0, t') + \hat{\xi}_1(t)$, $\hat{b}(L, t) = \int dt' G_2(t, t') \hat{b}(0, t') + \hat{\xi}_2(t)$, where $G_{1,2}(t, t')$ are the Green's functions relating the input and output operators in the SF and signal bands, respectively. $\hat{\xi}_{1,2}(t)$ describe the in-coupling of vacuum noise to each wavelength band, which can be determined by the requirement of preserving the commutation relation of the field operators at the waveguide output.

The above Green's functions can be rewritten using normal-mode decomposition in a fashion similar to the treatment of free-space diffraction [23]:

$$G_1(t, t') = \sum_{n=0}^{\infty} \zeta_n \phi_n(t) \psi_n^*(t'), \quad (2a)$$

$$G_2(t, t') = \sum_{n=0}^{\infty} \tau_n \varphi_n(t) \psi_n^*(t'), \quad (2b)$$

where $\psi_n(t)$ is the n -th eigenmode of the input signal, while $\phi_n(t)$ and $\varphi_n(t)$ are its corresponding output eigenmodes at the signal and SF wavelength, respectively. ζ_n and τ_n are the corresponding decomposition coefficients in descending order. In the Hilbert space defined by those eigenmodes, the input-output transformation relations for the signal are simply given by ($n = 0, 1, 2, \dots$)

$$\hat{a}_n = \zeta_n \hat{b}_n + \hat{\epsilon}_n, \quad (3a)$$

$$\hat{c}_n = \tau_n \hat{b}_n + \hat{\zeta}_n, \quad (3b)$$

where $\hat{b}_n = \int dt \hat{b}(0, t) \phi_n^*(t)$, $\hat{a}_n = \int dt \hat{a}(L, t) \psi_n^*(t)$, and $\hat{c}_n = \int dt \hat{b}(L, t) \psi_n^*(t)$ are the annihilation operators for the input signal, the output SF, and the output signal waves in their respective n -th normal modes. $\hat{\epsilon}_n$ and $\hat{\zeta}_n$ are the corresponding output-noise operators satisfying $[\hat{\epsilon}_n, \hat{\epsilon}_n^\dagger] = 1 - \zeta_n^2$ and $[\hat{\zeta}_n, \hat{\zeta}_n^\dagger] = 1 - \tau_n^2$. It is then clear that ζ_n^2 is the probability for an input photon in mode ψ_n to be up converted into mode ϕ_n , while τ_n^2 is the probability for it to be reshaped into mode φ_n without changing its color [24].

The Green's functions and hence their mode structures in Eq. (2), are determined by the phase matching property of the waveguide and the pump pulse shapes. By manipulating those two, it is possible to tailor both the temporal profiles of the eigenmodes and their coefficients. To this end, it was proposed that single-mode QFC can be achieved by engineering the group velocity of the pump wave to match that of either the signal or the SF wave while making it very different from the other [25, 26, 17]. This approach, however, is applicable to only a few optical materials at some specific wavelengths. In contrast, we propose to use appropriately shaped pump pulses

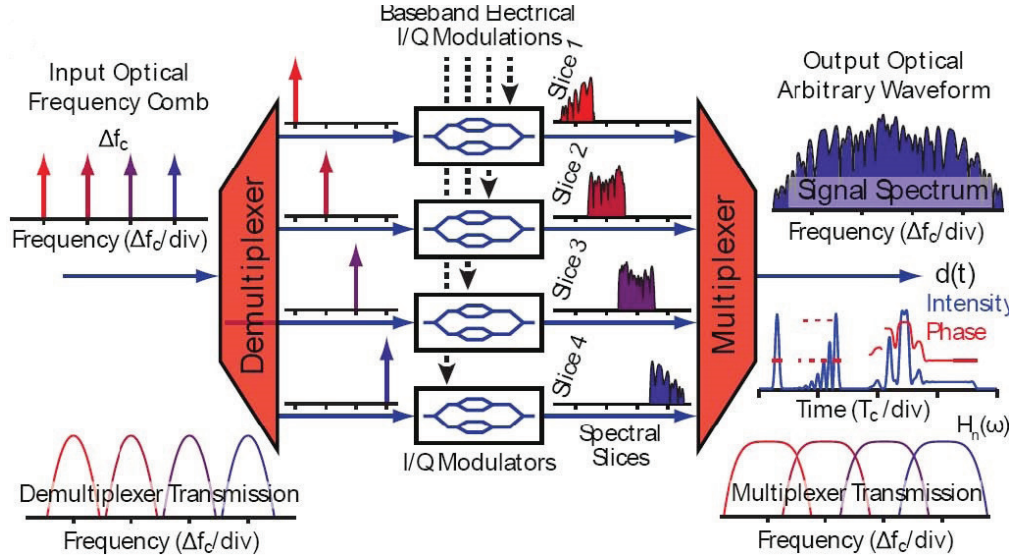


Fig. 2. Schematic of dynamic OAWG.

to avoid the aforementioned constraint on phase matching. Uniquely, implemented with the dynamic OAWG technique described in Section 3, it can achieve real-time management of the mode profiles and structures. This represents a new capability in quantum optics, allowing for, e.g., secure quantum communications in high dimensional Hilbert spaces.

3. Dynamic OAWG

In OAWG, line-by-line manipulation of a coherent OFC provides complete control of the temporal amplitude and phase of an optical waveform. As depicted in Fig. 2, the dynamic OAWG waveform-shaper spectrally demultiplexes each optical line of the frequency comb to separate spatial locations, applies phase and amplitude modulations to each line with an array of modulators, and then spectrally multiplexes the modulated comb lines to create the output waveform [8, 27, 28]. Based on time-frequency relationships, the OAWG device creates the desired temporal waveform when it correctly generates the waveform's complex spectrum. By coherently combining the modulated comb lines to synthesize a waveform's spectrum, we have enabled terahertz-bandwidth waveform generation while using only gigahertz-rate electronic signals. Thus, picosecond control of optical waveforms are feasible.

Any practical OAWG implementation must maintain the coherence between the lines of the OFC throughout their manipulation. Although this is possible with bulk-optic waveform shapers, monolithically integrated InP OAWG devices are a compact solution that includes high-speed modulators and spectral demultiplexer/multiplexers based on AWGs [27, 28]. The fidelity of the quantum operations resulting from the QFC process depends directly on the quality of the OAWG-generated pump waveforms [29]. Two primary sources of waveform-shaping errors, the input frequency comb noise and the nonideal OAWG device performance, determine the ultimate fidelity of the pump waveform. Naturally, the shaped waveform cannot have a signal-to-noise ratio (SNR) better than that of the input frequency comb whose SNR is limited by the total intensity noise and phase noise (timing jitter). However, with the availability of high quality OFC, electrical and optical limitations of the OAWG device typically determine the waveform-shaping performance. Finite optical crosstalk in the spectral demultiplexer and

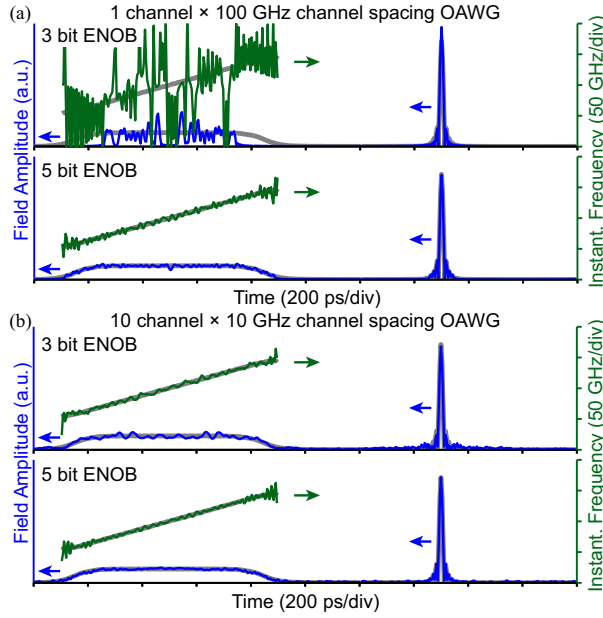


Fig. 3. A 100 GHz OAWG waveform simulation assuming (a) one-channel or (b) ten-channel OAWG device with different DAC performances (i.e., ENOB). The grey line is the target waveform, the blue line is the waveform amplitude (left and right are for chirped and transform-limited pulses, respectively), and the green line is the waveform's instantaneous frequency.

multiplexer is the primary optical impairment since it causes additional lines from the frequency comb to be present on each channel. This creates noise terms in the output waveform due to the unintentionally modulated lines. Thus, for a given total bandwidth of an OAWG device, B , and channel crosstalk value, C , the waveform's SNR decreases as the channel bandwidth decreases (i.e., additional required channels/comb lines) and goes as approximately $[C(N-1)]^{-1}$ where N is the number of channels or comb lines. For a given total bandwidth, increasing the number of channels requires increasing the multiplexer resolution and that generally increases its crosstalk.

The electrical impairments are primarily determined by the digital-to-analog converter (DAC) performance and the modulator's linearity and purity (e.g., if phase modulation results in unwanted amplitude modulation). A typical DAC performance metric is its effective number of bits (ENOB) which brings together all sources of noise and distortion that limit its usable resolution. A generated signal's electrical SNR (dB) is estimated from the DAC ENOB by $\text{SNR} = 6.02 \times \text{ENOB} + 1.76$ [30].

An OAWG device simulation is helpful to illustrate the waveform's fidelity improvement associated with improvements in DAC ENOB and an increasing number of channels when the waveform fidelity is only limited by the DAC performance. Figure 3(a) shows simulations of an output waveform created by a single-channel, 100-GHz OAWG device for three different DAC ENOB values. The grey line indicates the target or desired waveform and the blue line is output waveform amplitude, while the green line is the waveform chirp or instantaneous frequency. The single 2-ns duration target waveform consists of two pulses; the first is a linearly-chirped pulse (170-GHz/ns chirp rate) and the second is a transform-limited pulse. When a 3-ENOB DAC is used, the waveform has significant errors visible. Figure 3(b) shows the same waveform

generated with the same DAC, but with a 10-channel OAWG device. The improvement in waveform fidelity is apparent.

The example waveform in Fig. 3 also shows that some waveforms are “easier” to shape than others. Although both pulses have the same 100-GHz total spectral bandwidth (8th-order super-Gaussian), the chirped pulse is particularly sensitive to shaping errors while the transform-limited pulse is only slightly affected. These examples illustrate that to achieve a desired waveform bandwidth and fidelity; there is a tradeoff that must be optimized between the number of spectral slices (more complex optics for more slices) and the slice bandwidth (more complex electronics for broader slice bandwidth). In the following, we design our pump pulses within those practical constraints.

4. Example Applications

By tailoring the QFC process using shaped pump pulses produced by OAWG devices, novel operations can be achieved on quantum signals. Here, we present three examples valuable to quantum optical information processing. The first is mode-selective conversion of time-frequency modes, where out of 10 modes generated via spontaneous parametric downconversion (SPDC), an arbitrary single mode or a superposition of any two modes is up-converted with near unity efficiency while all other orthogonal modes are unconverted at the output. The second application is mode-resolved photon counting, in which the photon-number statistics of a quantum photonic signal is determined on a mode-to-mode basis. These two applications represent a new capability for measurement of quantum signals, which opens a door to, e.g., ultradense quantum coding utilizing overlapping spatial, temporal, and spectral modes. In the third application, an arbitrary quantum mode is deterministically reshaped into a different one with near perfect fidelity and almost no loss. This corresponds to an important resource for interfacing disparate photon sources, e.g., resonance fluorescence from a quantum dot with a heralded photon from a parametric down-conversion source. It is also essential for hybrid quantum networking, where signals in appropriate modes are crucial for achieving high performance [2, 31]. We numerically demonstrate the ability to immediately adapt tools designed for classical optical pulses for deterministic quantum optical manipulation and measurement. These numerical studies are supported by our experimental results presented in Section 5.

For all of those applications, we numerically identify the appropriate temporal shapes of pump pulses for given phase matching properties of the waveguide. For concreteness, in the following we consider a typical off-the-shelf 6-cm long waveguide with $\mu_1 = 2.54$ ps/cm and negligible group velocity dispersion [see Eq. (1)]. With telecom-band applications in mind, we consider both the signal and pump to be in the C-band with negligible group velocity mismatch, i.e., $v_n = 0$ for $n = 1, 2, \dots$. The desired SFG interaction is quasi phase-matched (QPM) via periodic poling. For simplicity, in this section we assume an ideal sinc^2 QPM profile. The pump pulses are created by utilizing an OFC with 30 lines spaced by 40 GHz as an input to an OAWG device. In practice, more comb lines are accessible and will give better performance. In order to determine the appropriate pump-pulse profile, we numerically optimize the amplitude and phase of each comb line using the standard random-walk optimization method [32].

4.1. Mode-selective quantum frequency conversion

Here we show how to use mode-selective quantum frequency conversion to select a single or a superposition of quantum modes. As an example, we consider the Schmidt modes of a two-photon state generated via phase-matched SPDC driven by 15-ps duration, fifth-order super-Gaussian pump pulses, whose output signal and idler photons are picked by rectangular 5.4-nm filters [33]. Three such modes are shown in Fig. 4.

By using the numerically optimized pump pulses, each of the signal modes can be selectively

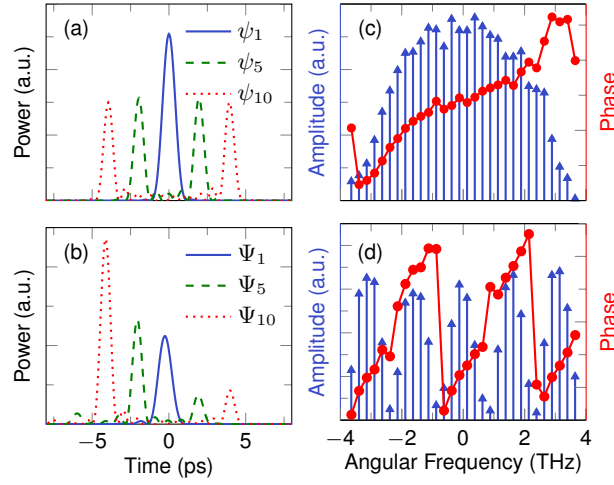


Fig. 4. (a): Temporal profile of the n -th Schmidt mode, ψ_n , of the SPDC-generated photon pairs. (b): Temporal profile of pump pulse Ψ_n optimized for selective upconversion of mode ψ_n . (c) and (d): Amplitude and phase profiles of comb lines for constructing Ψ_1 and Ψ_5 , respectively.

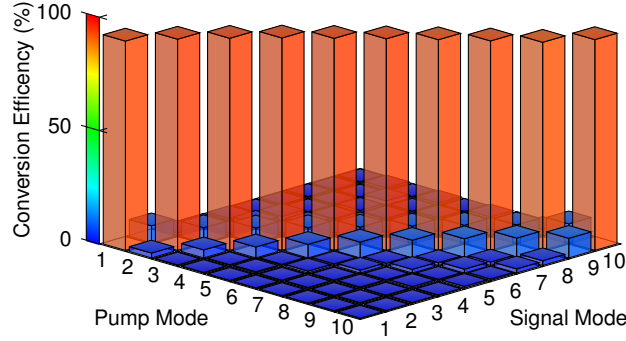


Fig. 5. Conversion-efficiency matrix for 10 SPDC modes, where the n -th pump mode is optimized to upconvert the n -th signal mode with high efficiency while avoiding converting the others.

upconverted. In Fig. 5, we plot the resulting conversion efficiencies for the first 10 modes, where the n -th pump mode (Ψ_n) is optimized such that the conversion of the n -th signal mode (ψ_n) is maximized while suppressing the conversion of the other 9 modes. As shown, any signal mode can be selectively upconverted with $> 90\%$ internal efficiency and with > 10 dB extinction ratio with respect to all the other modes. We define the extinction ratio as the ratio of the conversion efficiency of the desired mode to that of the maximum of the remaining 9 modes, $S_{ij}(\text{dB}) = 10 \log_{10} \frac{\eta_{ii}}{\max\{\eta_{ij}: j \neq i\}}$. We note that selectivity and extinction ratio are used interchangeably in the manuscript. In the expression of S_{ij} , the subscript 'i' represents the 'i-th' pump mode whereas the subscript 'j' represents the 'j-th' signal mode. In Fig. 4 (b)-(d), we plot the temporal profiles and the comb-line coefficients of several optimized pump pulses. We note that for typical lithium niobate or PPKTP waveguides, the peak power of those pump pulses is on the order of watts.

This approach can also selectively convert arbitrary superpositions of those modes. Consider, for example, the superpositions between mode 1 and 5: $\psi_{\pm} = \frac{1}{\sqrt{2}}(\psi_1 \pm \psi_5)$. The temporal profiles of those modes and the optimal pump pulses for converting each mode, Ψ_{\pm} , are plotted in Fig. 6(a) and (b), respectively. Notably, these pump profiles deviate significantly from $\Psi_1 \pm \Psi_5$, shown in Fig. 4(b). The resulting mode-selectivity is plotted in Fig. 6(c), where each of the superposition mode is upconverted with $> 90\%$ efficiency with over 10 dB extinction over other input modes. While the selective upconversion here assumes high-fidelity reconstruction of the pump using the OAWG device, we performed additional noise analysis by introducing intensity- and phase-errors to the pump-pulse. Our results (see Appendix A) show that the mode-selectivity remains robust to these errors.

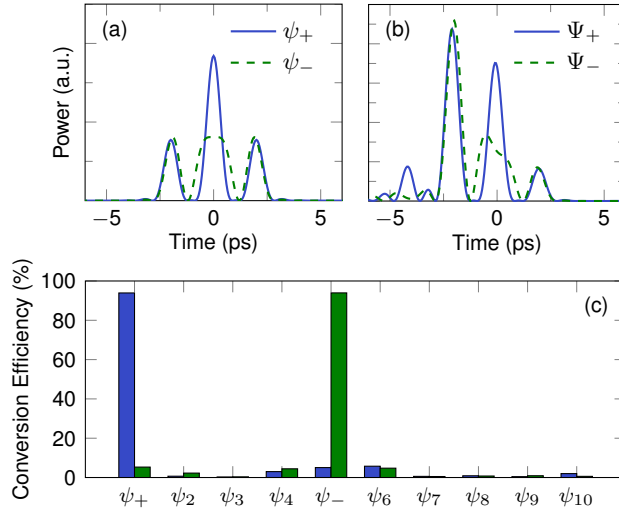


Fig. 6. (a) Temporal profiles of ψ_{\pm} . (b) Optimized pump-pulse profile $\Psi_{+(-)}$ for converting $\psi_{+(-)}$. (c) Conversion efficiencies of 10 orthogonal modes by Ψ_+ (blue bar) and Ψ_- (green bar), respectively.

4.2. Mode-Resolved Photon Counting

Next we consider mode-resolved photon counting realized by passing the quantum signal through a sequence of mode-selective QFC stages, as we conceptualized in Ref. [19]. The pump pulse for each stage is shaped by an OAWG device so as to selectively upconvert a single incoming mode that is orthogonal to the rest. After each stage, the mode profiles of the unconverted photons may be modified. However, all of them will remain nearly orthogonal with each other provided that the previous stages have high mode-selectivity. In the following stage, another pump pulse is optimized to selectively upconvert one of the (reshaped) modes. Continuing this sequence and counting the upconverted photons generated by each stage yields the photon-number statistics of the input signal in each time-frequency mode. For simplicity, we consider a two-stage QFC process for photon counting in two modes (ψ_1 and ψ_5) out of the 10 SPDC-generated modes in the previous section. QFC in the first stage is tailored identically to that in the single-stage case (c.f. Figs. 4 and 5). The pump pulse for the second stage is optimized to selectively upconvert mode 5 whose temporal shape is modified passing through the first stage. Fig. 7(a) shows the temporal profiles for both the pump and signal modes. Using this pump, 91.4% conversion efficiency is achieved for mode 5 with more than 15 dB extinction

from adjacent modes.

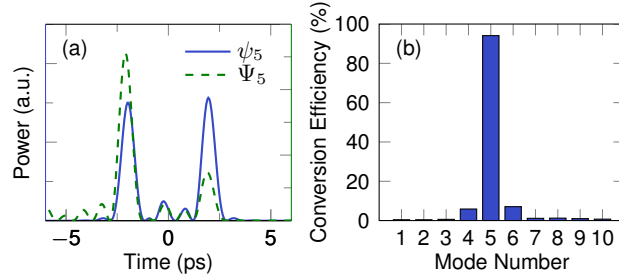


Fig. 7. (a) Temporal shapes of mode 5 after the first QFC stage (blue) and the pump pulse Ψ_5 for selectively upconverting it (green). (b) Conversion efficiencies by pump Ψ_5 .

4.3. Lossless Waveform Reshaping

In this subsection, we show that quantum modes can be reshaped without a color change using QFC. Previous methods for photon (re)-shaping were realized via direct phase and/or amplitude modulation, which is in practice accompanied by photon loss and often quantum decoherence as well [34, 13, 11]. This impairment renders these methods unsuitable for many loss-sensitive applications, particularly those for large-scale, deterministic quantum computing. In contrast, our QFC-based design can be in principle lossless and noise-free and thus provides a highly desirable solution for a wide range of quantum applications.

We first show reshaping of an exponentially decaying pulse, similar to quantum-dot emissions, into a Gaussian waveform. These waveforms represents an important resource for distributed quantum applications since they are robust against mode-mismatch-induced quantum

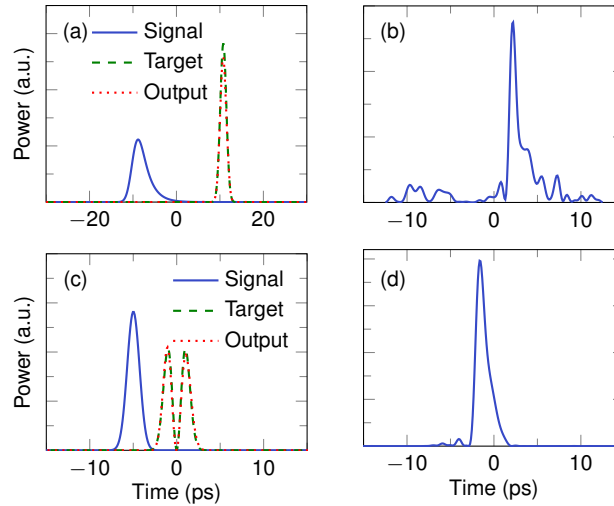


Fig. 8. (a) An exponentially decaying pulse is reshaped into a Gaussian waveform. The temporal profile of the pump pulse used is shown in (b). (c) A HG_0 mode is deterministically reshaped to a dual-peak HG_1 mode. The pump pulse profile is shown in (d).

distinguishability in photonic quantum circuits [35]. The two waveforms are shown in Fig. 8(a), where the conversion fidelity (i.e., the overlap of the resulting and target waveforms) is 93.6%. The designed pump pulse is shown in Fig. 8(b).

Second, we show mode transformation between Hermite-Gaussian (HG) modes, a class of widely deployed modes for quantum optical information processing. In Fig. 8(c), we reshape a single-peak, zero-order HG mode (HG_0) into a two-peak HG_1 mode. Using the tailored pump in Fig. 8(d), the resulting waveform matches with the target waveform by a conversion fidelity of $\gtrsim 99\%$, with 0.2% energy loss.

5. Experimental Investigations

In this section, we present an experiment demonstrating mode-selective SFG between waveform-shaped pump and signal pulses created by OAWG. The experimental results agree well with our theory's predictions.

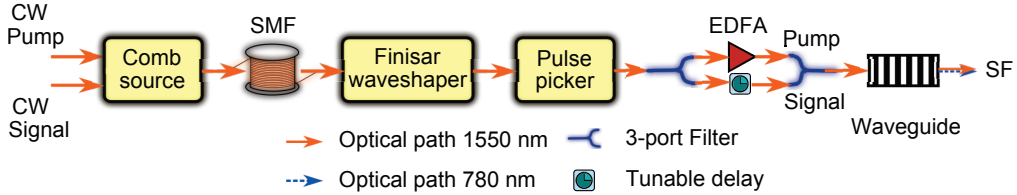


Fig. 9. Experimental schematic for mode-selective SFG.

The experimental setup is shown in Fig. 9, where cascaded phase and amplitude modulators [36] generate separate OFCs for the pump and signal using two continuous-wave lasers at 1561.9 nm and 1548.2 nm respectively. Transmission of the OFCs through ~ 300 meters of single-mode optical fiber offsets their phase chirp produced by the phase modulator, resulting in nearly transform-limited 2.3-ps pulses full-width at half-maximum (FWHM) for the pump and signal. Using the pulses as inputs to an OAWG device (Finisar Waveshaper 1000S) with an insertion loss of 4.5 dB, pump and signal in desired waveforms are generated using the comb-line parameters identified by our numerical model. Their amplitude and phase profiles are verified using a frequency-resolved optical gating (FROG) device. The pulse-repetition rate of the signal and pump is reduced from 20 GHz to 625 MHz using a pulse picker. The pump pulses are then amplified by an Er-doped fiber amplifier (EDFA) to acquire appropriate peak power specified by our simulation, while the signal pulses are temporally aligned with the pump using a tunable delay line. Finally, the pump and signal are combined and coupled into a fiber-pigtailed PPKTP waveguide (AdvR, Inc.), which is phase matched for SFG. We calculate the conversion efficiencies by observing the signal depletion at the waveguide output on an HP digital communication analyzer (DCA) with 30-GHz optical module.

Figure 10(a) shows the phase matching curve of the PPKTP waveguide, which is measured at 33°C with the pump wavelength at 1561.9 nm. As shown, it deviates significantly for the usual sinc-square profile for an ideal, uniformly periodic-poled waveguide. We model this non-ideality effectively by introducing higher-order group-velocity dispersion terms as shown in Eqs. (1), where coefficients μ_n are determined by fitting the measured phase matching data. Figure 10(b) shows the pump-power characteristic of the SFG efficiency, where 1.2 W of pump peak power is needed to achieve $\sim 80\%$ of conversion. Note that for the current waveguide, the highest internal conversion efficiency achieved is $\sim 80\%$, limited by the presence of multiple spatial modes for our wavelengths. The insertion loss of the fiber-pigtailed waveguide is ~ 4 dB.

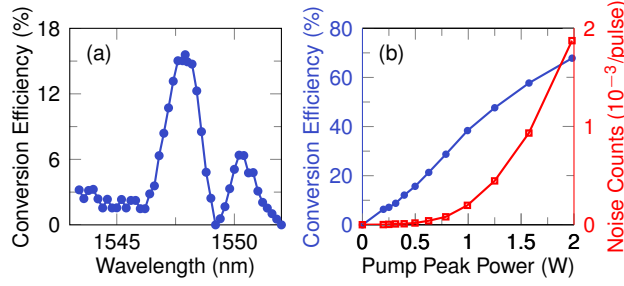


Fig. 10. (a) Phase-matching curve of the PPKTP waveguide used in Fig. 9. (b) The SFG conversion efficiency and the count rate of in-band noise photons versus the pump power.

For quantum applications, the level of in-band noise generated by the pump inside the waveguide must be low. In our system, noise photons are created in the SF band primarily through upconversion of Raman photons spontaneously scattered by the pump into the signal band [37]. To determine this noise level, we count noise photons created in a free-space coupled waveguide (identically fabricated as the one used in Fig. 9) pumped by a 160-ps pulse centered at 1550.7 nm. The noise photons are collected within 3-nm FWHM around the sum-frequency center wavelength (the signal is centered at 1560.8 nm). Our setup has a total maximum detection efficiency of 10% due to the transmission loss and the quantum efficiency of the single-photon detector. The measurement results are shown in Fig. 10(b), upon which we estimate that when the maximum SFG efficiency is reached, about 0.002 noise photons will be detected per pump pulse. Because the effective detection spectral width $B \gtrsim 1.2$ angular THz (determined predominantly by the waveguide’s phase matching) and the temporal of detection window $T = 160$ ps (prescribed by the pump pulse), there are more than $BT/4 \sim 50$ time-bandwidth modes being detected in this experiment [38]. Hence, operating in the single-mode regime (required for mode-selective operations), our system will detect $< 4 \times 10^{-5}$ noise photons per measurement, which is comparable with dark counts of typical InGaAs detectors for telecom-band photons. We expect to further reduce this noise level by using a longer-wavelength pump.

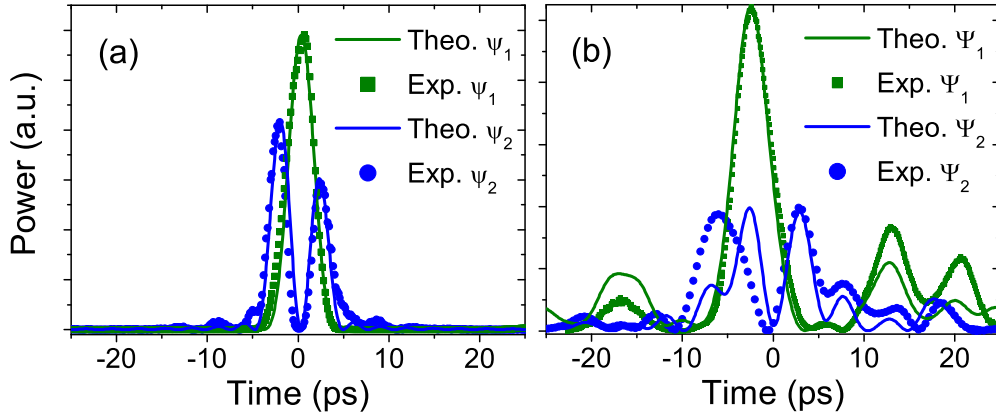


Fig. 11. Designed and measured signal (a) and pump (b) pulses for the mode-selective SFG experiment.

To demonstrate mode-selective SFG, we produce two overlapping signal pulses of orthog-

onal profiles, $\psi_{1,2}$, using an OAWG device with 17 input comb lines of 20-GHz spacing. For those signals, we design two pump pulses, $\Psi_{1,2}$, using the same OAWG device, each optimized to selectively up-convert ψ_1 or ψ_2 . The designed and measured signal and pump pulses are plotted in Fig. 11. The FROG measurements for the pump-pulse shapes are further explained in Appendix B.

Table 1 lists the simulated (η_{theo}) and measured (η_{exp}) SFG efficiencies for different combinations of the signal and pump pulses in Fig. 11. We find the measured SFG efficiencies by noting the undepleted and depleted signal powers on the DCA, also listed in the same table. We note that the simulation results have accounted for the highest-achievable conversion efficiency of $\sim 80\%$ due to the presence of multiple spatial modes in our waveguide. S_{theo} and S_{exp} are the theoretical and experimental mode selectivities, defined here for the 2-by-2 case as the ratio of the fractional conversion of a signal mode by its optimized pump to that of the other signal mode by the same pump. As seen, our experimental results agree well with our theory's predictions in all cases, which verifies our theory. For pump Ψ_1 , a selectivity of 8.4 dB is achieved, which is limited by the number of comb lines and the non-ideal phase matching of our waveguide with our theory's predictions.

Table 1. Signal conversion efficiencies for different pumps

P/S	Undepleted signal (mW)	Depleted signal (mW)	η_{theo} (%)	η_{exp} (%)	S_{theo} (dB)	S_{exp} (dB)
1/1	0.895 ± 0.004	0.295 ± 0.003	69.6	67.0 ± 0.5	8.3	8.4
1/2	0.990 ± 0.010	0.894 ± 0.004	10.2	9.7 ± 1.3		
2/1	0.990 ± 0.010	0.766 ± 0.002	20.5	22.6 ± 1.0	4.9	4.2
2/2	1.050 ± 0.003	0.428 ± 0.003	63.8	59.2 ± 0.4		

6. Conclusion

By incorporating quantum frequency conversion with classical optical arbitrary waveform generation, we have demonstrated numerically and experimentally a variety of all-optical tools for manipulating and measuring high-speed quantum signals, ideally without loss or decoherence. Considering realistic device parameters, we have shown via simulation selective upconversion of an arbitrary single mode or superposition of modes, including the selection of any 10 individual temporal modes generated in a spontaneous down-conversion source. We have also shown arbitrary reshaping of quantum signals with near-unity fidelity and essentially no loss, a functionality that is highly desirable for interfacing disparate quantum systems. Using a dynamic OAWG device, our technique can allow for realtime manipulation and measurement of quantum signals, enabling applications such as high-speed quantum-state tomography of high-dimensional signals [39] and adaptive measurement of spatiotemporal profiles of quantum light [40]. Experimentally, we have discriminated two overlapping signals using commercial OAWG and waveguide devices, demonstrating mode-selective frequency conversion with over 8 dB selectivity. We expect to achieve higher selectivity by using more comb lines for OAWG. In addition, we have characterized the background noise level of the waveguide and determined that such devices are suitable for quantum operations with both the pump and signal in the telecom C-band. Our technology could open doors to new regimes of operation in quantum optics, particularly in quantum information processing requiring efficient and low-loss operations on fast photonic signals.

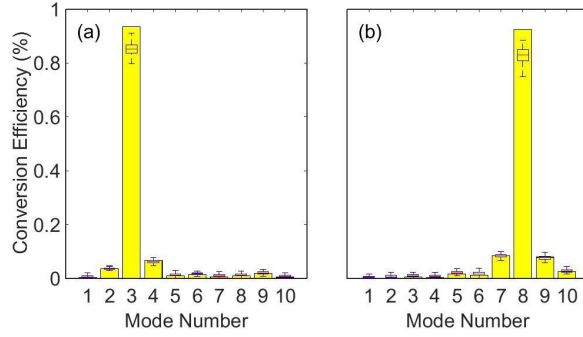


Fig. 12. Yellow bars show the conversion efficiencies for modes 1 through 10 using a pump optimized for mode 3 in (a) and that for mode 8 in (b). (a) The box and whisker plots on each column show the results of 99 trials of noise added to the pump optimized for mode 3. The red line shows the mean conversion over 99 trials, the box edges show the 25th and 75th percentiles of the set and the whiskers extend to include 99% of the data set. Anything outside of the whiskers is considered an outlier. (b) The box and whisker plots on each column show the results of 99 trials of noise added to the pump optimized for mode 8. The red line shows the mean conversion over 99 trials, the box edges show the 25th and 75th percentiles of the set and the whiskers extend to include 99% of the data set.

This research was supported in part by the DARPA Quiness program (Grant # W31P4Q-13-1-0004) and by the NSF (Grant # ECCS-1232022).

Appendix A: Effects of intensity and phase noise on mode-selectivity

In order to verify the robustness of the OAWG-enabled QFC technique, we performed simulations by adding intensity and phase-noise to the frequency combs that were used to optimize the pump-pulse shapes. The conversion efficiencies for the mode set in Fig. 4 were calculated with normally distributed random perturbations added to each pump comb line. The mean of the distribution is equal to the comb line amplitude, c_i for $0 \leq i \leq N$, where N is the total number of comb-lines, and has a standard deviation $\sigma = 0.05c_i$. Similarly, phase perturbations were applied with a standard deviation $\sigma = 0.05 * 2\pi$ (18 degrees). We performed 99 trials using noisy pumps and the conversion efficiencies for each mode were calculated and recorded. The mean and standard deviation of each mode's conversion efficiency were calculated for the set of 99 trials. Here, we show the effects of the amplitude and phase noise on a lower- and higher-mode, Fig. 12. For the third mode the optimized conversion efficiency (Fig. 4) was 93.5%, which reduced to $85 \pm 0.91\%$ when the noise was added to the pump. Similarly, the eighth mode had a conversion efficiency of 92.4% and reduced to $83 \pm 0.9\%$ in the presence of noise. With 5% noise added to each comb line phase and amplitude, the mean conversion for the selected modes reduced by 8–10%. In spite of the decrease in conversion efficiency for individual modes, the mode-selectivity remained robust to these perturbations, and remained above 10 dB for modes 1 through 8, 9.8 dB for mode 9, and 9.7 dB for mode 10. Furthermore, comparing the noisy pump pulse shape to the optimized pump pulse yielded an overlap of 91%. We believe that these intensity- and phase-errors can be suppressed to below 5% in the experiment, and our analysis here highlights the robustness of our technique to this level of error.

Appendix B: FROG retrieval errors

We used a commercial FROG device (Southern Photonics HR 150) to characterize the pump and signal pulses in both intensity and phase. After we measured the FROG spectrograms with 512 number of wavelength points and 512 number of delay points with an integration time of 500 ms, we retrieved the pulses with a Fourier grid of $N \times N$ where $N = 128$ or 512 . The retrieval software (Femtosoft Technologies) consisted of several retrieval algorithms working simultaneously to minimize the retrieval errors. We obtained retrieval errors for the four pulses as 1.31×10^{-3} (ψ_1), 8.75×10^{-3} (ψ_2), 8.62×10^{-3} (Ψ_1) and 2.15×10^{-2} (Ψ_2). We expected the retrieval errors to be less than 5×10^{-3} for simpler pulses like ψ_1 whereas retrieval errors as high as 9×10^{-3} for more complex pulses like ψ_2 and Ψ_1 were still considered to produce reliable results [41]. The unusually high retrieval error for Ψ_2 indicated that the measured waveform was substantially less reliable. The systematic errors involved in performing this measurement are under investigation.

Once we obtained the retrieved pulses, we shifted them appropriately along the time axis to align their peaks to those of the simulated pulses. We also normalized the retrieved pulses to the same scale as the simulated pulses to note the quality of the pulses produced. We quantified the latter via the overlap defined as $\eta_{ov} = \frac{|\int E_{sim}^* E_{frog} dt|^2}{\int |E_{sim}|^2 dt \int |E_{frog}|^2 dt}$ where E_{sim} and E_{frog} were the field intensities for the simulated and FROG-retrieved pulses, respectively. We obtained 96.5% overlap for ψ_1 , 94.2% for ψ_2 , 95.3% for Ψ_1 and only 69.3% for Ψ_2 . We believe the poor overlap was partially due to the high retrieval error for Ψ_2 .